Breaking Wave Imaging using Lidar and Sonar

Oscar Bryan, Paul M. Bayle, Christopher E. Blenkinsopp, and Alan J. Hunter, *Senior Member, IEEE*

***Abstract*—The two-phase flow generated from breaking ocean waves plays a crucial role in various geophysical processes, including dissipation of wave energy and atmospheric gas exchange. This paper presents a technique to measure the two-phase flow generated by breaking waves at prototype scale. We have demonstrated the validity and potential of this technique in the Large Wave Flume (Grosser Wellenkanal, GWK) facility in Hanover, Germany. Actively breaking, depth-limited waves were measured using an array of three downward-looking lidars mounted above the water surface and an upward-looking multibeam sonar below. This novel setup enabled the characterisation of the complete upper boundary (free water surface and splash-up) and seaward lower boundary (entrained cavity and bubble plume) of the breaking wave. We have quantified the migration of the lower boundary as the cavity and plume are entrained in the water column – penetrating towards the seabed, moving onshore with the passage of the wave crest, and then rising as it is slowly advected offshore. We have also estimated the overall composition of the splash, cavity, and plume as the breaking wave evolves over time. Our observations are consistent with results from previous small-scale laboratory experiments and the suitability of the technique for experimentation at prototype scale has been demonstrated.**

***Index Terms*—Breaking waves, two-phase flow, sonar, lidar**

I. Introduction

WAVE breaking in shallow water is a phenomenon that has long been a subject of fascination within both the scientific and non-scientific communities. Wave breaking on beaches leads to dissipation of incident wave energy and is a driver for a range of nearshore processes including sediment suspension and transport, nearshore circulation, bar formation and wave runup (e.g [1], [2], [3], [4]. Upon breaking, the wave overturns generating a splash-up and entraining a plume of air bubbles. Thus, after wave breaking there exists a continuum of time-dependent void fractions α, bounded by the upper surface of the splash where $\alpha \rightarrow 1$ and the lower boundary of the evolving bubble plume where $\alpha \rightarrow 0$.

In plunging breaking waves, which are common on intermediate to dissipative beaches [5], a jet is formed as the wave overturns and encloses a cavity of air (commonly called a breaking wave vortex, e.g. [6], [7], [8]) between the underside of the jet and the front face of the wave. After the overturning jet strikes the surface water ahead of the wave at the plunge point (e.g. [9]), air is entrained into the water column beneath the surface water due to two primary mechanisms [10]: 1) formation of larger bubbles (diameter $D > 2$ mm) by the fragmentation of the air cavity or vortex [10]; and 2) entrainment of smaller bubbles by the impact and subsequent splashing of the overturning jet and in the shear layer between the jet and the water in the preceding trough [11]. Once entrained, the bubbles form a plume which is driven rapidly down into the water column after which it disperses as bubbles are advected by turbulence and wave-generated currents, and rise back to the surface [12].

Entrainment of air by breaking waves has been shown to influence physical processes, including air-sea transfer of gases [13], generation of sea-surface sound [14], and the production of the sea-salt aerosol [15]. As a consequence, many researchers have investigated the aerated regions generated by breaking waves in both the laboratory and the field. In the field, the majority of quantitative measurements have been confined to bubble clouds in the open ocean which were defined by Deane [16] as the remnants of the high air fraction plumes that are generated during active wave breaking. These field measurements have primarily focussed on the measurement of bubble size distributions (e.g. [17], [14], [18]) or void fractions (e.g. [19], [20]) using acoustic or optical methods. Investigation of active bubble plumes during and directly after breaking waves is less common as such plumes are acoustically and optically opaque, and the location of breaking waves in the field is highly variable, making it difficult to locate an instrument to adequately capture the entrainment and subsequent evolution of the bubble plume. Obtaining high-quality measurements of the production and evolution of the bubble plumes beneath actively breaking waves is important for our understanding of the wave breaking process and the process of air entrainment [21]. Bubble plume entrainment has been shown to contribute significantly to the energy dissipated during wave breaking [22], active bubble plumes are thought to contribute to air-sea gas transfer [13] and such data is needed for the validation of multiphase models of wave breaking (e.g. [23]). Smith [24], [25] used an upward-looking multibeam system in deep water breaking waves and found that it was possible to acoustically image the underside of the bubble plumes generated by actively breaking wave crests. In the nearshore, Deane and Stokes [11], [26] took a specially designed optical system into the surf zone of a natural beach to examine bubble formation mechanisms and measure bubble size distributions during the early moments of breaker generated plumes. As with breaking wave geometry, the majority of investigations of breaker generated plume measurements have been undertaken in the laboratory using conductivity-based sensors (e.g. [22], [27]), optical methods (e.g. [28]) and optical fibre probes (e.g. [29], [30], [31]). In particular Lamarre and Melville [22] and Blenkinsopp and Chaplin [30] investigated bulk characteristics of breaker generated bubble plumes in small-scale laboratory wave flumes including the time-variation of bubble plume depth, horizontal position and volume.

Due to the short duration of the breaking process and the

O. Bryan, P. Bayle, C. Blenkinsopp, and A. Hunter are with the University of Bath, Claverton Down, Bath BA2 7AY, North East Somerset, United Kingdom; e-mail: a.j.hunter@bath.ac.uk.

highly variable location of the break point on natural beaches, quantitative measurements of the water surface during breaking have been obtained almost exclusively at small-scale in laboratory wave flumes using video imagery obtained through the flume wall. These studies have primarily investigated the nature of wave breaking (e.g. [32]), the breaking wave vortex geometry (e.g. [7], [8]) or other geometrical properties of breaking waves such as the plunge and splash distances (e.g. [33], [34]). In additional to video-based studies, recent work by Smith et al. [35] has examined the potential for X-ray methods to capture the evolving shape of very small-scale overturning waves and wave breaking has also been studied using numerical methods (e.g. [36], [37]). While multiple researchers have investigated the potential to determine wave heights in the field from oblique, shore-based video imagery, quantitative measurements of the water surface in the field at a resolution suitable for investigating the changing shape of waves during the breaking process have only recently been made possible thanks to the development of LiDAR (Light Detection And Ranging) technology for the measurement of water surface elevation. Martins et al. [38] deployed an array of three lidars along a shore-perpendicular pier and obtained measurements of the water surface elevation as it varied in time at a spatial resolution of centimetres from the break point to the runup limit at a sandy beach in North East England. It should be highlighted that while this approach provides detailed measurements of the changing wave geometry, the lidars are only able to capture the upper surface of the overturning jet and subsequent splashes generated by breaking waves.

The splash generated by a breaking wave is perhaps the most impressive visual aspect of waves breaking on our coastlines, often reaching heights greater than that of the incident wave. These splashes contribute to energy dissipation [30] and bubble entrainment [39], and are a significant feature of breaking waves that must be reproduced in computational models of the breaking process. Despite this, there have been few investigations and even fewer measurements of the splash process to date meaning that current understanding is limited. Peregrine [40] presented a simple one-dimensional model of the splash-up process. Several laboratory experiments (e.g. [41], [39], [42], [43], [44], [45]) have used video imagery to capture the splash generated by small-scale breaking waves and demonstrated that upon falling back to the water surface, the initial splash-up generated by the overturning motion pushes up a smaller secondary splash-up. This secondary splash-up is projected forward before falling back to the water surface where it creates strong vortex-like motions and generates another, smaller jet-splash cycle. This process has also been observed in the results of numerical models of the wave breaking process (e.g. [36]), and Jansen [39] showed that as many as eight of these jet-splash cycles may occur before the organised motion completely breaks down. In their study of void fractions both above and below the water surface of small-scale depth-limited breakers, Blenkinsopp and Chaplin [30] measured the temporal evolution of breaker generated splash-up characteristics including splash volume and found that the splash process accounted for at least 2.5 to 5% of the energy dissipated during breaking in their test cases. To the authors' knowledge, quantitative data on breaker generated splashes at field scale is currently lacking.

This study presents a novel technique that allows measurements of the upper and lower envelope of the rapidly evolving two-phase flow generated by actively breaking depth-limited waves obtained in prototype-scale breaking waves in a large-scale laboratory wave flume. Novel data are obtained via a combined approach to image the upper surface of the splash using an array of downward-looking LiDAR (Light Detection And Ranging) instruments suspended above the water surface synchronised with measurements of the lower/seaward surface of the evolving bubble plume obtained using an upward-looking multibeam SoNAR (Sound Navigation And Ranging) instrument.

II. Methodology

A. Experimental Facility and Instrumentation

1) Wave Flume: The data presented in this paper was collected as part of the larger DynaRev experiment which was completed to investigate natural and engineered coastlines in a rising sea-level. The experiment took place in the Large Wave Flume (Grosser Wellenkanal, GWK) in Hannover, Germany, during August and September 2017. The flume measures $309\ \mathrm{m}$ long, $5\ \mathrm{m}$ wide and $7\ \mathrm{m}$ deep [46] and is shown in Figure 1. A sandy beach with a median grain size of diameter $D_{50} = 0.33\ \mathrm{mm}$ was installed with an initial plane slope of 1:15. This initially planar slope was reshaped by wave action to form a barred profile. The coordinate system was defined as follows: the vertical elevation, z is defined positive upwards from the base of the flume; the cross-shore coordinate system has its origin at the wave paddle and is positive in the direction of the beach. A combined piston-flap-type wave paddle was used to generate irregular waves with a significant wave height $H_s = 0.8\ \mathrm{m}$ at the wave paddle and peak period, $T_p = 6\ \mathrm{s}$. The water depth was $4.9\ \mathrm{m}$. The individual wave analysed in Section III corresponds to the first wave of a test run and thus propagated and broke in unaerated water. The breaker height, H_b was approximately $1.1\ \mathrm{m}$ and it is assumed that the waves measured in the flume are homogeneous in the cross-flume direction. It is noted that a small wave caused by the ramping up of the wave paddle breaks prior to the arrival of the wave of interest and generates a small bubble plume with its seaward boundary at $x = 234\ \mathrm{m}$. However this plume is landward of the seaward boundary of the bubble plume analysed below and is not expected to influence the results presented.

2) Mechanical Profiler: A mechanical profiler was used to measure the sandy beach profile. The profiler consists of a mechanical roller attached to an overhead trolley which runs along a gantry on the flume side walls, as shown in Figure 3a. The system enables measurements of the complete bed profile to approximately $1 - 2\ \mathrm{cm}$ vertical accuracy.

3) Lidars: An array of three SICK LMS 511 lidar scanners was used to measure the time-varying water surface elevation along an $80\ \mathrm{m}$ transect on the flume centreline. All three lidars were sampled by a single computer at a scan rate of $25\ \mathrm{Hz}$ and angular resolution of $0.166\ \mathrm{deg}$. However, the data from the lidars were downsampled to $10\ \mathrm{Hz}$ to match the sonar

Fig. 1: Waves breaking in the GWK flume.

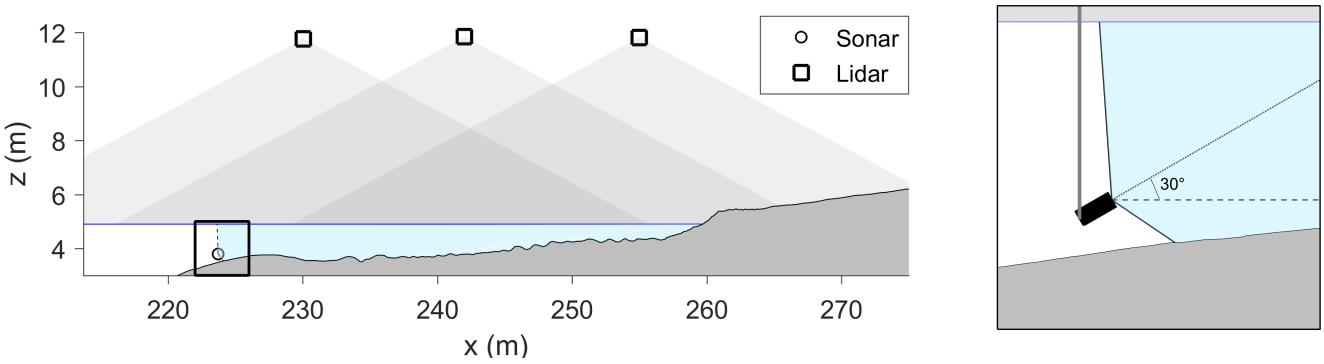

(a) (b)

Fig. 2: Laboratory and equipment setup, showing: (a) sonar and lidar positions within the flume; and (b) a close-up of the sonar configuration.

scan rate. Each lidar is capable of obtaining measurements within a 190 degree field of view, though here we consider only the central 150 degrees within which valid water surface measurements were obtained. The lidars were mounted to the flume roof at $z = 11.80$ m, (6.9 m above the still water line) at cross-shore locations $x = 230$ m, $x = 242$ m and $x = 255$ m and looked vertically down. The installed lidar array is shown in Figure 3b and illustrated in Figure 2a. Note that when used to measure breaking and broken waves in the setup described here, the lidar instruments detect the upper boundary of the water/splash/air-water mixture.

4) Sonar: A Reson SeaBat 7125 multibeam echo-sounder was used to image the underwater bubble plumes generated by the breaking waves. This instrument operates at a frequency of 400 kHz. It has an opening angle of 128 deg and a 0.54 deg beam divergence angle. Operating parameters were tuned in baseline still water conditions (c.f., Figure 4) to maximise data quality; this lead to a transmitter power of 195 dB, receiver gain of 44 dB, a frame rate of 10 pings/s, and a corresponding maximum range of 25 m. The frame rate was selected by qualitatively optimizing the trade-off between reverberation noise and temporal resolution. The acoustic intensity levels were not calibrated for this device and, therefore, only the relative measurements are considered in this work. The instrument was mounted on a vertical arm fixed to the overhead trolley of the mechanical profiler. The receiver was oriented in the vertical plane and aligned centrally along the length of the flume (the instruments are shown in Figure 3c). The cross-shore location was adjusted by moving the trolley along the flume walls and the deployment depth and orientation angle were also adjustable. A range of different cross-shore locations, depths, and angles were tested to optimise observability of the plume. A final deployment angle of 30 deg above horizontal looking towards the beach was selected so that the opening angle would cover the seaward edge of the breaker generated plumes (Figure 2b). For the data presented in this paper, the instrument was positioned at $x = 223.7$ m across-shore, $y = 0$ m along-shore (on the flume centreline), and $z = 3.8$ m in elevation, as illustrated in Figure 2a. Note that when used to measure breaking and broken waves in the setup described here, the

(a)

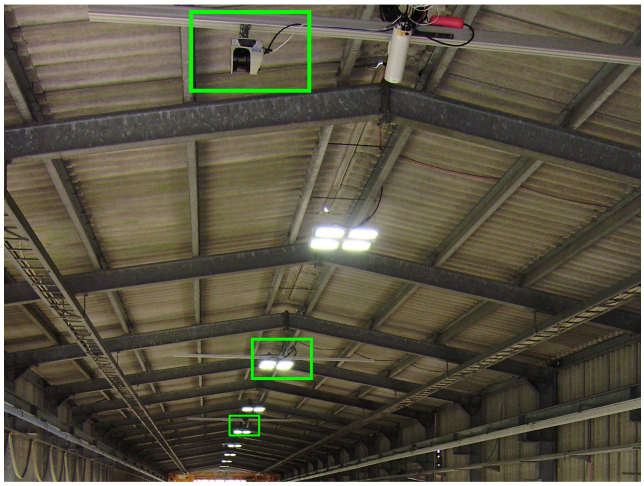

(b)

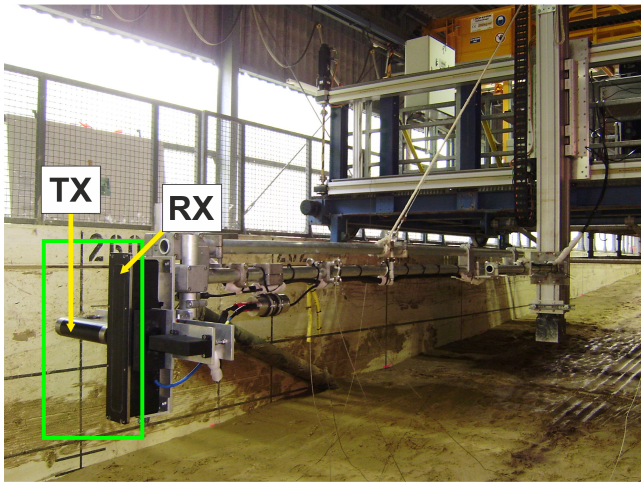

(c)

Fig. 3: Instrumentation: (a) trolley and mechanical profiler; (b) fixed roof deployment of the three SICK lidars; and (c) adjustable pole mounting of the Reson Seabat 7125 multibeam sonar from the trolley, with the transmitter (TX) and receiver array (RX) indicated. Note that the pole is shown in its horizontal position for mounting / adjusting the sonar and was lowered to its vertical position for the measurements.

sonar detects the pre-breaking water surface and the lower-seaward boundary of the evolving bubble plume.

B. Data Processing

1) Synchronisation and co-registration: During the experiment, all data collection computers were time-synchronised over a local area network to a common time server. In order to correctly align the lidar data from all three instruments, the exact position and orientation of each lidar was established by measuring fixed targets at known locations within the flume. The position and orientation of the sonar was established by measuring the horizontal and vertical offset from the known gantry position. The temporal and spatial synchronisation of data from the lidar array and sonar was confirmed visually by observing animations of the data from multiple waves passing through the measurement region. The maximum synchronisation error is expected to be half a time-step at the sonar scan rate, i.e., $\leq$ 50 ms. Sonar data corresponding to the region above the water surface were removed based on measurements from the lidar array. These data represent secondary reflections which are not straightforward to interpret and they have, therefore, been masked. The synchonised and co-registered data are shown in Figure 5. The data from the three different lidars are indicated in different colours and the acoustic back-scatter intensity measured by the sonar has been expressed in dB relative to the maximum recorded value over all of the frames.

2) Measurement of Cavity/Plume Boundary: The sonar data were processed semi-automatically to detect and track the seaward boundary of the combined cavity / plume region. This enabled measurement of the boundary's spatiotemporal migration and the variation of its acoustic backscatter intensity. For each frame, the procedure was initiated using a manual selection of two points on the observed boundary – one at the top near the water surface and another at the bottom towards the bed. A straight line fit was made through the two selected points and rectangular windows were distributed uniformly in depth along its length between the water surface and the bed. For the results in this paper, one hundred windows of width 2 m were used. Histograms of the acoustic intensity were formed within each of the windows and a minimum intensity threshold was used to check whether the backscatter level exceeded the noise floor. For the windows where this condition was met, a percentile threshold relative to the window's maximum intensity was used to demark the plume boundary. The other windows were excluded and used to delimit the vertical bounds. In this work, a minimum intensity threshold of -26 dB and a percentile threshold of 95% were selected based on a qualitative assessment of performance. These parameters were tuned to provide robust detection for the current data set and will need to be retuned for alternative data. This procedure is illustrated in Figure 6

3) Segmentation of Two-Phase Flow Regions: The two-phase flow that is generated during a wave breaking event can be segmented into three distinct regions: 1) the *cavity* of air beneath the overturning wave; 2) the *plume* of aerated water caused by the penetrating jet; and 3) the *splash* above

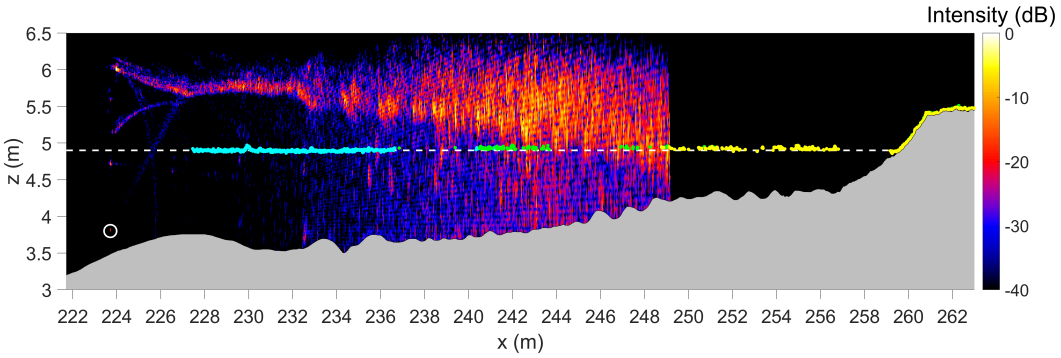

Fig. 4: Baseline lidar and sonar measurements during still water conditions. The water surface measurements from each lidar are shown in green, cyan and yellow for the seaward, middle and landward lidars respectively. Sonar backscatter intensity is plotted on a 1 cm grid and is represented by the colourmap. The still water level ($z = 4.9$ m) is represented by the dashed white line. The sonar position is shown by the white circle. The sand bottom measured by the mechanical profiler is represented by the grey region.

the water surface (see Figure 7). We have taken steps to make an approximate segmentation of these three regions from the synchronised lidar and sonar data. The seaward boundary of the combined cavity/plume region is estimated using the method presented in Section II-B2 and the water surface elevations of the breaking wave surface and splash are obtained directly from the lidar measurements. The area between these two boundaries is not measured. However, by making simple assumptions for their expected geometry based on images from the work of Blenkinsopp & Chaplin ([30], Figure 4; hereafter BC4) and taking the simplest approach of projecting straight lines between well-defined regions of the flow, the approximate areas of the cavity, plume, and splash regions can be estimated. To this end, we have taken the following steps. The upper boundary of the splash region is measured directly by the lidar array, while the underlying water surface is assumed to define the lower boundary. This lower boundary is occluded by the splash. As a first-order approximation, the boundary is defined here by a straight line between defined features in the data: the seaward turning point in the lidar data between the overturning jet and the splash; and the point where the splash meets the undisturbed water surface in front of the wave. The underwater boundary estimated from the sonar measurements is assumed to be caused initially by the formation of the cavity and is consistently curved in shape. The occluded part of the cavity boundary can be approximated as two straight lines that connect to the aforementioned turning point in the lidar measurements between the overturning jet and the splash. This is illustrated in Figure 7a. Transition from the cavity to plume is assumed to occur when the curved underwater boundary is observed to straighten and the acoustic intensity changes from a sharp reflection to diffuse scattering. We assume that the cavity transitions quickly into the plume and there is only a short period of time when a partial cavity and partial plume co-exist. The occluded part of the plume boundary is approximated by connecting straight lines from the observed boundary edges to the features previously defined to delineate the seaward and landward boundaries of the splash region. This is illustrated in Figure 7b. We acknowledge that this is a crude approach as it is limited by the fact that we are unable to observe the landward boundary of the plume, or the boundary between cavity / plume and splash. Nonetheless it provides an indication of the evolution of the main structures observed within the two-phase flow and is expected to capture trends in the evolving areas of these features.

III. Results

A. Breaking Wave Visualisation

Synchronised and co-registered data from the profiler, lidars, and sonar are plotted during still water conditions in Figure 4 and at several key times during a breaking wave in Figure 5, illustrating the measurements obtained from above and below water. The complete data set can be viewed in the animation that accompanies this paper, which is available on IEEE Xplore.

As previously observed in the field by Martins et al. [38] it is evident that the lidar array provides the capability to measure the evolving water surface at a spatial resolution of the order of cm. This is sufficient to capture complex features of the breaking process, including the upper surface of the flow as the wave overturns and produces subsequent splash-up cycles. The water surface measurements from the lidar array are complemented by the sonar data which also captures the changing water surface from below and matches well with the lidar. In addition, the sonar is able to detect the boundary of the evolving aerated regions generated during the breaking process, including the cavity and plume. In this case, the relative position of the sonar meant that only the seaward boundary of these regions was observed. Thus, the combination of lidar and sonar measurements enable the above and below-surface features of the two-phase flow generated by an actively breaking wave (including cavity, plume, and splash) to be measured at prototype scale for the first time.

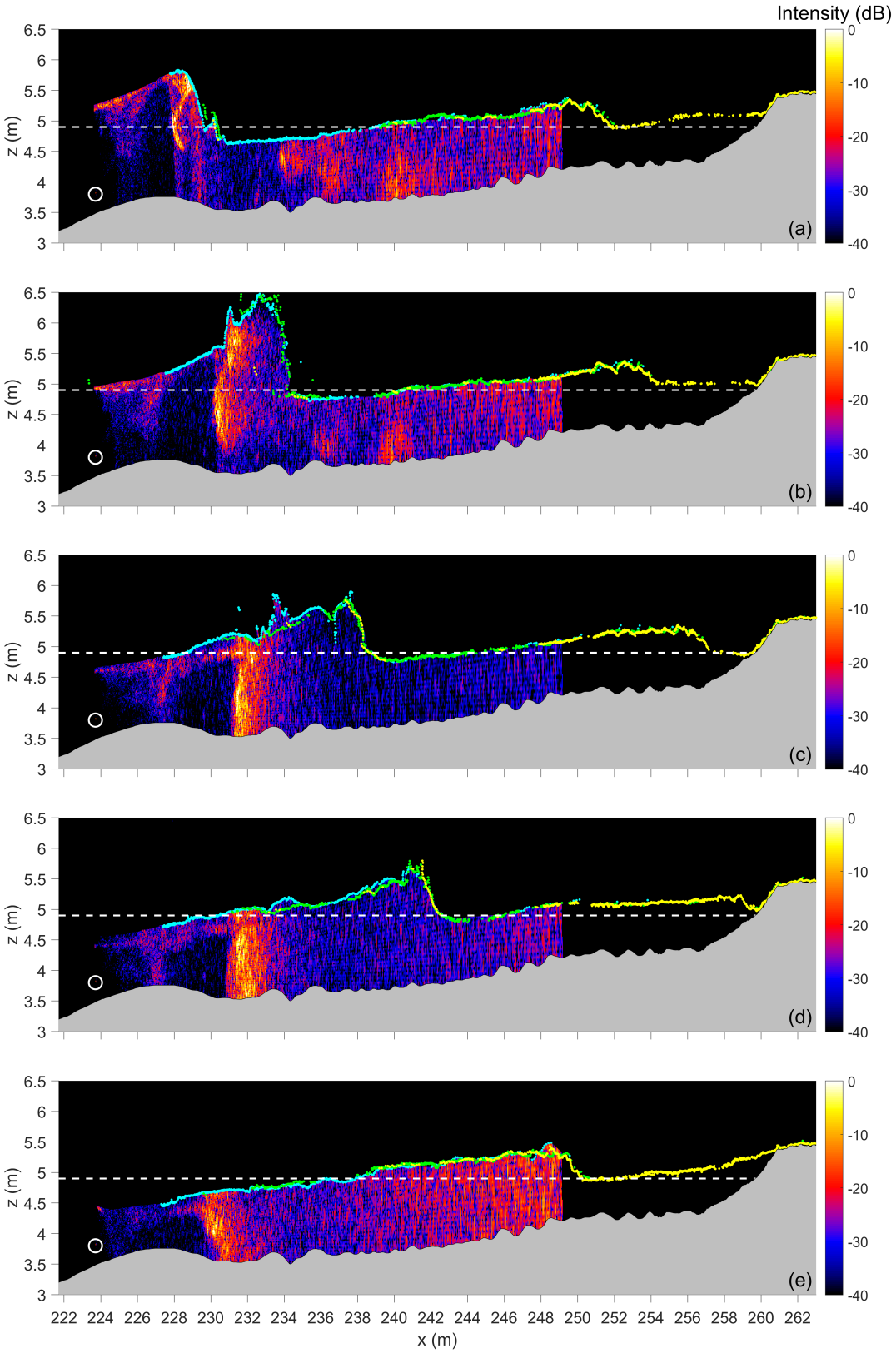

Fig. 5: Sonar and lidar measurements at key times during a breaking wave event: (a) initial overturning; (b) primary splash-up; (c) plume reaching the bed; (d) plume intensity peak raising from mid depth to the near surface; (e) plume fading and moving offshore before the next wave. The sonar measurements above the water surface are caused by multipath reflections and do not represent meaningful measurements in this region. Therefore, this region has been coloured black to aid readability of the figure. The complete data set can be viewed in the accompanying animation available on IEEE Xplore.

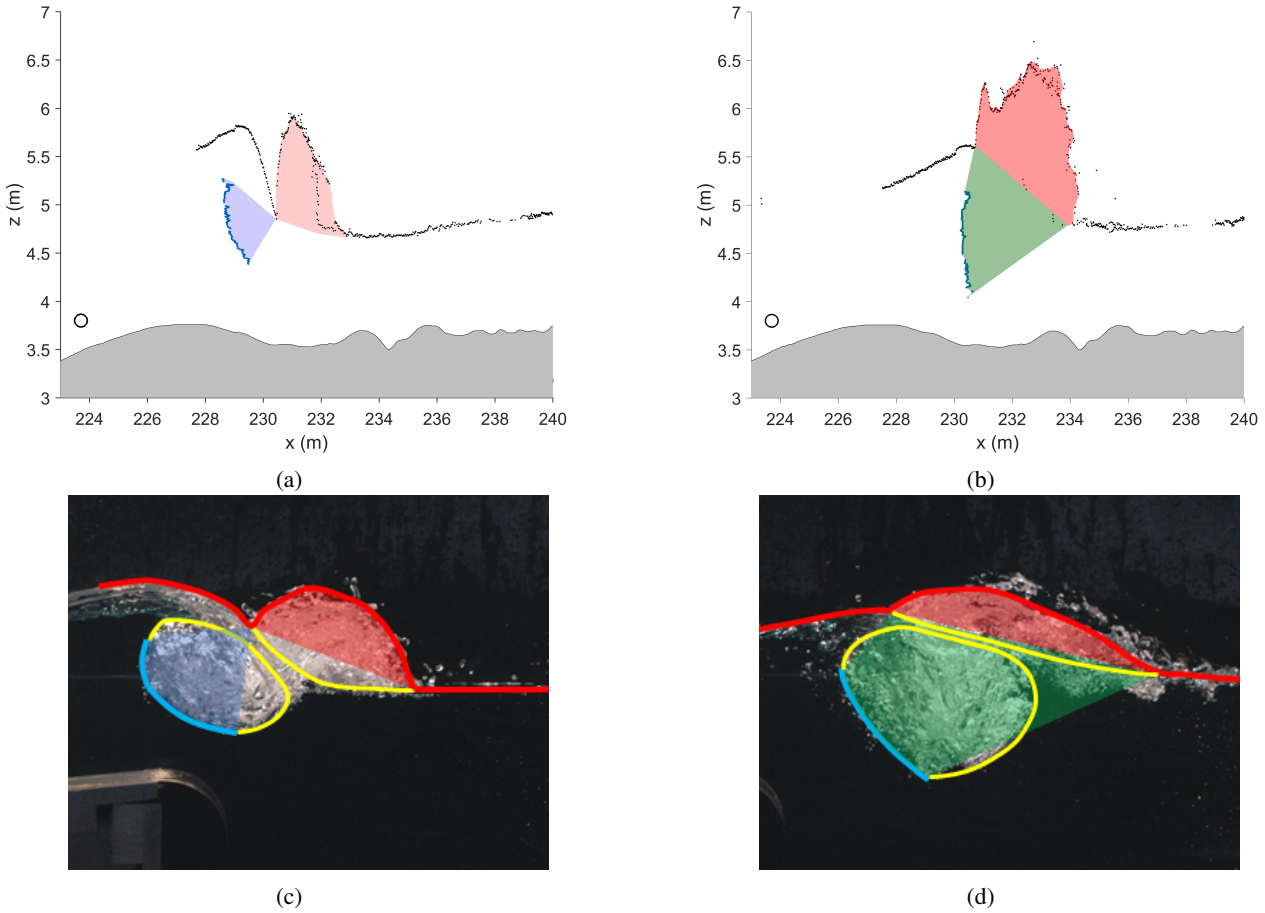

Fig. 7: Illustration of the approximate cavity / plume / splash segmentation procedure on: (a,b) the current work, where the black and blue dots show the lidar and sonar measurements, respectively; and (c,d) photographs of small scale breaking waves from BC4, where the yellow curves show the observed boundaries and the red and blue curves show the expected equivalent boundaries that would be measured by lidar and sonar. In each case, the red, blue, and green areas are the approximate segmentation of splash, cavity, and plume regions.

The sequence of breaking wave measurements is described below and compared to the laboratory visualisations presented in BC4. It should be noted that the waves presented there broke over a truncated reef structure into deep water (approximately $7H_b$) which meant that generated bubble plumes were unaffected by the bed. In the current experiment, the penetration of the bubble plume is restricted by the presence of the bed. Additionally, the waves shown in BC4 were observed to be more strongly plunging than that analysed in the current paper, though it is noted that the values of the surf similarity parameter are comparable ($\xi_{b,\text{current}} = 0.38$ vs $\xi_{b,\text{BC4}} = 0.48$) and indicate weakly plunging waves in both cases [5]. Further validation could be made against the theoretical models for plunging waves, e.g., [9].

Figure 5a shows the wave as it initially overturns at $x = 228$ m. It is evident that the curved feature observed in the sonar image between $x = 228$ m and 229 m and $z = 4.5$ m and 5.7 m is the smoothly curving underside of the water surface as the wave overturns (also observed in BC4(a)), while the lidar detects the upper surface of the overturning jet. The region between these two surfaces enables an estimate of the cavity volume per unit width as discussed in Section III-C. It is noted that the overturning jet has impacted with the wave trough and there is evidence of the initial stages of splash generation around the water surface between $x = 230$ m and 231 m. In Figure 5b, the primary splash is fully developed (compare to BC4(c)) and can be observed to extend from the wave crest at $z = 5.6$ m to a peak elevation of 6.5 m, which is almost twice the breaking wave height. The curved shape of the initially entrained cavity is still evident but observed to be driven deeper in the water column and we speculate that the less defined cavity boundary suggests that the initial cavity has begun to break up into smaller air pockets and bubbles to form a plume. Figure 5c can be compared to BC4(g)). A secondary splash-up is evident between $x = 237$ m and 239 m, formed by the impact of the primary splash as it falls back to the water surface. The plume has now formed and been driven further into the water column, reaching the flume bed. In Figure 5d, the base of the plume remains at the flume bed. In Figure 5e, it is evident that the seaward plume boundary has moved back towards the wave paddle, advected by seaward flow velocities associated with the passage of the wave trough.

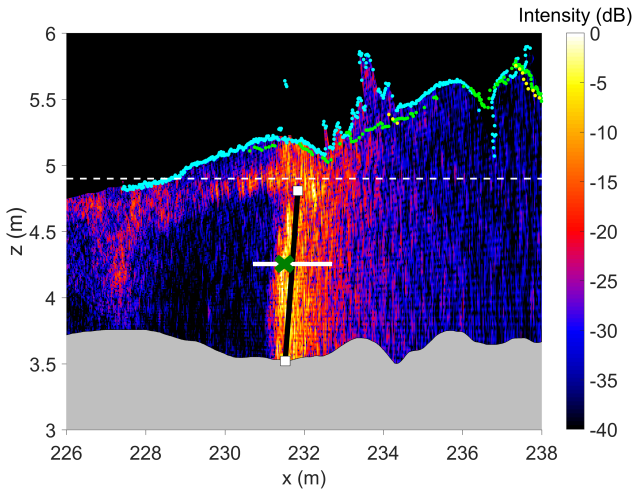

(a)

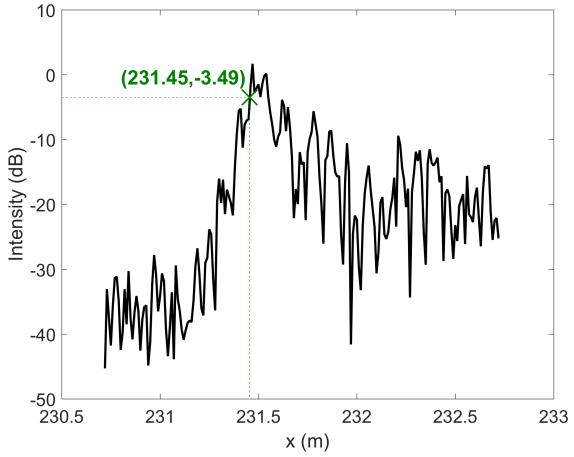

(b)

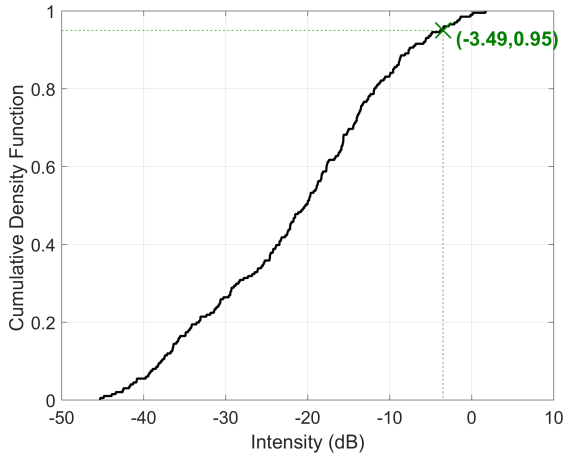

(c)

Fig. 6: Illustration of the detection procedure for the underwater boundary: (a) manually defined line approximation and 1 of 100 2 m-wide windows distributed along its length; (b) measured acoustic backscatter intensity within the window; and (c) associated cumulative density function. The 95th percentile is used to define the boundary and is indicated by the green crosses.

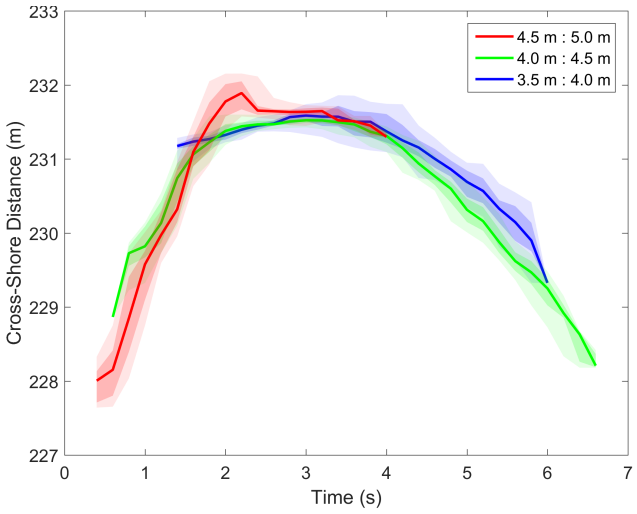

Fig. 8: Cross-shore migration of the bubble plume's offshore boundary for depths in the ranges $4.5-5$ m (red), $4-4.5$ m (green), and $3.5-4$ m (blue); the solid lines are the median positions and the shaded regions show the 50 and 90-percentiles.

The acoustic back-scatter intensity is reduced throughout the plume suggesting rising and dispersion of the plume bubbles as the next wave approaches. It is noted however that while the acoustic backscatter of the plume is decreasing, we might expect significant number of bubbles and suspended sediment to remain in the water column and these obscure the acoustic detection of the following waves.

B. Evolution of the Cavity / Plume Boundary

By estimating the boundary as described in Section II-B3, the horizontal movement of the seaward boundary of the cavity / plume during the breaking event can be tracked. Furthermore, the acoustic backscatter intensity along this boundary can be measured. In the present work, uncalibrated intensity measurements were made at a single frequency. However, further development using calibrated measurements at multiple frequencies, will provide an opportunity to characterise small-scale properties of the plume, such as the bubble size distribution and density [47], [19].

Figure 8 presents the mean horizontal position of the cavity / plume seaward boundary relative to the wave paddle within three different vertical bands: $z = 5.0$ m to 4.5 m, 4.5 m to 4.0 m and 4.0 m to 3.5 m. Also plotted are the 50th and 90th percentiles of the cross-shore distance which indicate that the uncertainty in the mean boundary position; these remain approximately constant and are smaller than 0.5 m throughout. When initially entrained, bubbles are only present in the upper depth band ($z = 5.0$ m $- 4.5$ m). As the depth of the plume increases, the plume boundary is detected in the lower bands. From $t = 4$ s only the lower bands are present as the wave trough passes above the seaward boundary of the plume and the upper band lies above the water surface. For the first 2 seconds, the boundary moves onshore at an approximately constant speed of 2.3 m$/s$. This is slightly slower than the wave celerity of 2.8 m$/s$ predicted by linear wave theory for

a water depth (wave trough to bar crest) of 0.8 m. Similar behaviour was observed by Blenkinsopp and Chaplin ([30], Fig 7) who found that the centroid of bubble plumes generated by small-scale laboratory breakers moved at or slightly below the velocity predicted by linear theory during the entrainment phase. Between $t = 1.7$ s and 2.7 s, it is observed that the bubbles in the upper layer move more rapidly landward than those in the lower bands consistent with higher wave generated landward flow velocities at the surface (e.g. [48]). The majority of air entrainment occurs during passage of the wave crest. Once the crest has passed beyond the seaward boundary of the bubble plume around $t = 4$ s, the entrained bubble plume is advected offshore by the predominantly seaward directed flow velocities as associated with the wave trough. The peak offshore flow velocity is measured just before the next breaking wave arrives and is estimated to be approximately 1.8 m$/s$. This is comparable to the peak horizontal flow velocity at mid-depth predicted by linear theory of 1.89 m$/s$ and of the same order of magnitude as the peak offshore velocity of 0.9 m$/s$ measured 10 cm above the bed at $x = 233.5$ m (3 m to 5 m landward of the plume boundary position) by an electromagnetic current meter. Figure 8 presents the mean horizontal position of the cavity / plume seaward boundary relative to the wave paddle within three different vertical bands: $z = 5.0$ m to 4.5 m, 4.5 m to 4.0 m and 4.0 m to 3.5 m. Also plotted are the 50th and 90th percentiles which indicate that the uncertainty in the mean boundary position; these remain approximately constant and are smaller than 0.5 m throughout. When initially entrained, bubbles are only present in the upper depth band ($z = 5.0$ m $- 4.5$ m). As the depth of the plume increases, the plume boundary is detected in the lower bands. From $t = 4$ s only the lower bands are present as the wave trough passes above the seaward boundary of the plume and the upper band lies above the water surface. For the first 2 seconds, the boundary moves onshore at an approximately constant speed of 2.3 m$/s$. This is slightly slower than the wave celerity of 2.8 m$/s$ predicted by linear wave theory for a water depth (wave trough to bar crest) of 0.8 m. Similar behaviour was observed by Blenkinsopp and Chaplin ([30], Fig 7) who found that the centroid of bubble plumes generated by small-scale laboratory breakers moved at or slightly below the velocity predicted by linear theory during the entrainment phase. Between $t = 1.7$ s and 2.7 s, it is observed that the bubbles in the upper layer move more rapidly landward than those in the lower bands consistent with higher wave generated landward flow velocities at the surface (e.g. [48]). The majority of air entrainment occurs during passage of the wave crest. Once the crest has passed beyond the seaward boundary of the bubble plume around $t = 4$ s, the entrained bubble plume is advected offshore by the predominantly seaward directed flow velocities as associated with the wave trough. The peak offshore flow velocity is measured just before the next breaking wave arrives and is estimated to be approximately 1.8 m$/s$. This is comparable to the peak horizontal flow velocity at mid-depth predicted by linear theory of 1.89 m$/s$ and of the same order of magnitude as the peak offshore velocity of 0.9 m$/s$ measured 10 cm above the bed at $x = 233.5$ m (3 m to 5 m landward of the plume boundary position) by an electromagnetic current meter.

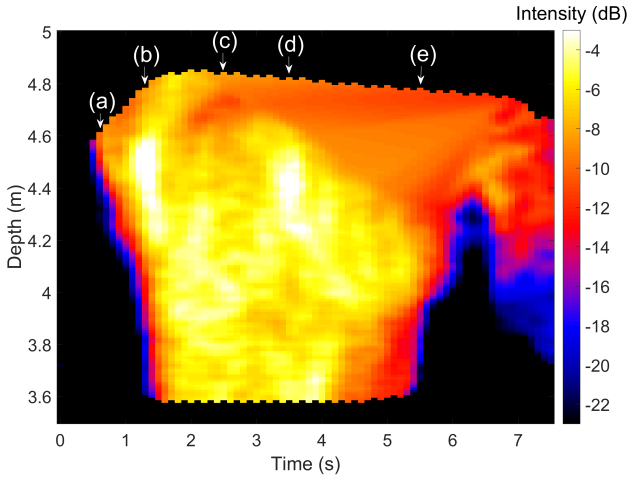

Fig. 9: Acoustic backscatter intensity along the detected cavity / plume boundary in a Lagrangian frame of reference as a function of depth and time. The labelled white arrows correspond to the associated frame in Figure 5.

Acoustic backscatter intensity measured along the estimated cavity / plume boundary is presented in Figure 9 in a Lagrangian frame of reference as a function of depth and time. This figure shows the injection and subsequent rise of the cavity and plume with key times labelled (a) to (e).

Strong acoustic backscatter that is not associated with the water surface is initially detected as the cavity captured by the overturning jet forms at (a) and is subsequently driven rapidly down through the water column over approximately 1 second between (a) and (b) when it reaches the bed. Previous observations in the laboratory by Blenkinsopp and Chaplin [30] and Lamarre and Melville [22] would suggest that the initial large air volumes that form the cavity are broken up into smaller bubbles to form a plume as the aerated region penetrates through the water column, though this cannot be observed directly in the present measurements. During the following period from (b) to (e), lasting approximately 4 seconds, bubbles are detected throughout the water column as the plume evolves due to bubble breakup, advection by currents, bubble rise and dispersion. Following point (e), the base of the remaining plume is observed to rise from the bed at a rate of approximately 0.5 to 0.75 m$/s$ before the arrival of the aerated flow from the next wave. The aerated flow generated by the subsequent (second) wave is less clear due to masking by the remaining bubbles from the first wave. By the third wave, the level of ambient bubbles in the water column makes acoustic imaging of the bubble plumes almost impossible.

Strong peaks in intensity are observed between (b) and (d). It is unlikely that these are caused by bubble resonance because the expected bubble diameters are distributed in the range $50 - 2500$ μm (e.g. [31]) corresponding to resonance frequencies in the range 3 kHz to 140 kHz [49] and the sonar is operating at 400 kHz, well outside this range.

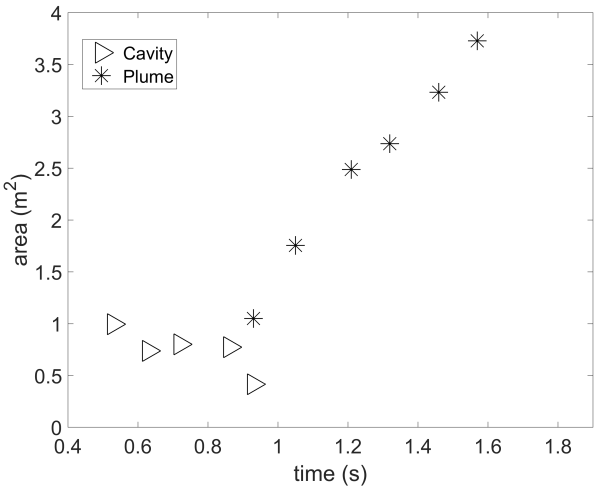

(a)

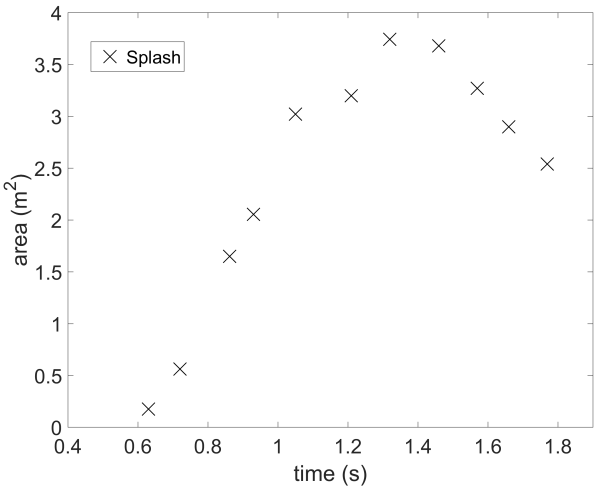

(b)

Fig. 10: Temporal evolution of the estimated areas of the cavity, plume, and splash.

C. Evolution of the Two-Phase Flow Regions

Figure 10 presents the temporal variation of the volume per unit width of the cavity, plume and splash features as defined in Section II-B3. Because the current method only detects the seaward side of the cavity and plume and the transition between cavity and plume is ill-defined, it is acknowledged that these estimates are crude but are useful to provide an indication of the temporal evolution of these features.

The cavity is a shortlived feature as the large air volumes initially entrained beneath the overturning jet rapidly break-up into smaller bubbles leading to a more disperse plume feature. The measurements presented here indicate that once formed, its volume remained approximately constant for 0.25 s, followed by a sudden decrease as the plume became dominant. The volume per unit width of the plume increases approximately linearly, consistent with the observations of Blenkinsopp and Chaplin [30] and Lamarre and Melville [22] in small-scale laboratory waves. The observed increasing volume is consistent with an initially high void fraction and low volume plume which increases in cross-sectional area as the base of the plume moves down through the water column, and the horizontal extent increases as bubbles are advected landward. It was not possible to estimate the decay of the plume volume in the current measurements due to the break down of the assumptions used to estimate plume volume from the landward-facing sonar. However Blenkinsopp and Chaplin [30] observed an exponential decay. Future work could deploy a second, seaward-looking sonar to enable these measurements and indeed improve on the other volume measurements presented here.

While Blenkinsopp and Chaplin [30] and Lamarre and Melville [22] observed a linear increase in plume volume per unit width with time, their measurements indicated that the peak volume, normalised by the initial cavity volume enclosed beneath the overturning jet obtained from images was between 1.0 [22] and 1.6 [30]. It is not clear whether the peak plume volume is measured in the current measurements as it was not possible to detect the subsequent plume decay, nonetheless the current measurements indicate a normalised peak volume of at least 3.75. This much larger plume volume in the current experiment is expected to be mainly due to differences in the nature of wave breaking (less intensely plunging waves) leading to a smaller peak cavity volume, greater uncertainty in the estimate of the peak cavity volume and potentially scale effects. The volume of splash per unit width is observed to increase as the primary splash-up is generated and is projected vertically up and landwards, followed by a decrease as it falls under the influence of gravity. This evolution is similar to that observed by Blenkinsopp and Chaplin [30]. However they estimated peak splash volume normalised by the initial cavity volume enclosed beneath the overturning jet to be between 1.25 and 1.6 whereas this value is 3.85 in the current measurements. It is noted that the peak splash and plume volumes measured in the current experiment are very similar, and this was also observed by Blenkinsopp and Chaplin [30].

IV. Conclusions and Future Work

In this paper, synchronised laboratory measurements of the time-varying water surface and bubble plume boundary in actively breaking, depth-limited waves were obtained at prototype-scale. An array of downward-looking lidar scanners were able to measure the rapidly varying surface profiles during wave shoaling, overturning and subsequent splashing. The lower, seaward boundary of the bubble plume generated by the breaking process was imaged acoustically by an upward-looking sonar. While further validation is needed, these measurements have demonstrated the potential to use this approach to obtain new information about the behaviour of the bubble plume and splashes generated by actively breaking waves at prototype-scale. The strength of our method is that we can observe the combined above water and underwater boundaries of the two-phase flow at high temporal resolution. A limitation is that only the boundaries that are within line of sight to the sonar can be observed. However, this can be addressed in future work by using multiple sonar sensors.

Based on some simple assumptions, it was possible to segment and investigate the bulk movements of the air cavity,

plume and splash regions of the flow. It was observed that the overall evolution of the bubble plume and splash was comparable to that observed in previous small-scale laboratory measurements by Blenkinsopp & Chaplin [30], [31]. In common with these measurements, it was observed that the bubble plume boundary moves landward after breaking at a speed slightly lower than the wave celerity predicted by linear theory. The volume per unit width of the plume increased approximately linearly as the plume was driven down to the bed and dispersed and the approximate rise speed of the bubble plume was consistent with that predicted by Leifer et al [50].

The experiment described here clearly demonstrates the potential of the combined lidar/ sonar methodology to obtain measurements in a highly complex and difficult to measure flow and has demonstrated that the bulk behaviour of bubble plumes and splashes generated in prototype-scale breaking is comparable to that at small-scale. Future work will use the method to investigate a wider range of wave conditions and breaker types using an optimised instrument configuration and more advanced data analysis method in a wave flume. An array of landward and seaward-looking sonar devices should be deployed to ensure adequate coverage of the entire bubble plume boundary and a wider frequency bandwidth to capture the bubble scattering characteristics. Calibrated backscatter intensity measurements at multiple frequencies should be used to estimate useful properties of the bubble plume, including bubble size distribution and density. The ability to image the complete bubble plume and splash boundaries opens up the potential to relate the bubble plume and splash properties to the wave parameters, potentially enabling bubble plume / splash characteristics to be inferred based purely on wave measurements. Controlled lab testing provides the opportunity to overcome real world issues associated with instrument deployment and contamination of the acoustic data due to remnants of precious and subsequent waves. Leading on from a successful detailed lab study and overcoming these issues, the methodology developed here has the potential to obtain valuable measurements of active breaking waves in the field.

ACKNOWLEDGEMENT

This work was supported financially by the European Union's Horizon 2020 Research and Innovation Programme under grant no. 654110, HYDRALAB+. Oscar Bryan and Alan Hunter were further supported by a University of Bath Alumni Fund grant. Paul Bayle's PhD research is supported through a studentship from the EPSRC Water Informatics, Science and Engineering (WISE) Centre for Doctoral Training. We would like to thank staff at the Large Wave Flume (Grosser Wellenkanal, GWK), in particular Matthias Kudella and Stefan Schimmels for making the experiment a success. We also thank members of the DynaRev project team who provided assistance in the laboratory: Isabel Kelly, Emily Gulson, Daniel Conley, Gerd Masselink, Rafael Almar, Ad Reniers, Peter Troch, David Gallach-Sanchez, Robert McCall, Ian Turner, Tom Baldock, Peter Ganderton, Tom Beuzen, Gwyn Hennessey, Huub Rijpers and Aril Pandya.

REFERENCES

[1] T. Aagaard and B. Greenwood, "Suspended sediment transport and morphological response on a dissipative beach," *Continental Shelf Ressources*, vol. 15, pp. 1061–1086, 1995.

[2] P. Bonneton, N. Bruneau, B. Castelle, and F. Marche, "Large-scale vorticity generation due to dissipating waves in the surf zone," *Discrete and Continuous Dynamical Systems - Series B*, vol. 13(4), pp. 729–738, 2010.

[3] F. Hoefel and S. Elgar, "Wave induced sediment transport and sandbar migration," *Nature*, vol. 299(5614), pp. 1885–1887, 2003.

[4] H. F. Stockdon, R. A. Holman, P. A. Howd, and A. H. Sallenger, "Empirical parameterization of setup, swash, and runup," *Coastal Engineering*, vol. 53, pp. 573–588, 2006.

[5] J. A. Battjes, "Surf similarity." 14th International Conference on Coastal Engineering, 1974, pp. 466–480.

[6] S. T. Mead and K. Black, "Predicting the breaking intensity of surfing waves," *Special Issue of the Journal of Coastal Research on Surfing*, pp. 103–130, 2001.

[7] C. E. Blenkinsopp and J. R. Chaplin, "The effect of relative crest submergence on wave breaking over submerged slopes," *Coastal Engineering*, pp. 967–974, 2008.

[8] B. Robertson, "Wave vortex parameters as an indicator of breaking intensity," *International Journal of Physical and Mathematical Sciences*, no. 1, pp. 47–54, 2013.

[9] M. S. Longuet-Higgins and E. D. Cokelet, "The deformation of steep surface waves on water. a numerical method of computation," *Proceedings of the Royal Society of London*, pp. 1–26, 1976.

[10] G. B. Deane and M. D. Stokes, "Scale dependence of bubble creation mechanisms in breaking waves," *Nature*, vol. 418, pp. 839–844, 2002.

[11] ——, "Air entrainment processes and bubble size distributions in the surf zone," *Journal of Physical Oceanography*, vol. 29, pp. 1393–1403, 1999.

[12] G. de Leeuw and I. Leifer, "Bubbles outside the plume during the luminy wind-wave experiment," *Gas Transfer at Water Surfaces*, vol. 127, pp. 295–301, 2002.

[13] W. K. Melville, "The role of surface-wave breaking in air-sea interaction," *Annual Review of Fluid Mechanics*, vol. 28, no. 1, pp. 279–321, 1996.

[14] G. Deane, "Sound generation and air entrainment by breaking waves in the surf zone," *Journal of the Acoustic Society of America*, vol. 102, pp. 2671–2689, 1997.

[15] D. C. Blanchard, "The electrification of the atmosphere by particles from bubbles in the sea," *Progress in Oceanography*, vol. 1, pp. 73 – 202, 1963.

[16] G. B. Deane, "The performance of high-frequency doppler sonars in actively breaking wave crests," *IEEE Journal of Oceanic Engineering*, vol. 41, pp. 1028–1034, 2016.

[17] H. Medwin, "In-situ acoustic measurements of bubble populations in coastal ocean waters," *Journal of Geophysical Research*, vol. 75, pp. 599–611, 1970.

[18] H. Czerski, M. Twardowski, X. Zhang, and S. Vagle, "Resolving size distributions of bubbles with radii less than 30 m with optical and acoustical methods," *Journal of Geophysics Research*, vol. 116, 2011.

[19] S. Vagle and D. M. Farmer, "A comparison of four methods for bubble size and void fraction measurements," *IEEE Journal of Oceanic Engineering*, vol. 23, pp. 211–222, 1998.

[20] R. S. Al-Lashi, S. R. Gunn, and H. Czerski, "Automated processing of oceanic bubble images for measuring bubble size distributions underneath breaking waves," *Journal of Atmospheric and Oceanic Technology*, vol. 338, pp. 1701–1714, 2016.

[21] K. T. Kiger and J. H. Duncan, "Air-entrainment mechanisms in plunging jets and breaking waves," *Annual Review of Fluid Mechanics*, vol. 44, no. 1, pp. 563–596, 2012.

[22] E. Lamarre and W. K. Melville, "Air entrainment and energy dissipation in breaking waves," *Nature*, vol. 351, pp. 469–472, 1991.

[23] G. Ma, F. Shi, and J. T. Kirby, "A polydisperse two-fluid model for surf zone bubble simulation," *Journal of Geophysical Research: Oceans*, vol. 116, no. C5.

[24] J. A. Smith, "Acoustically observed bubble cloud evolution under deep-water breaking waves," *Journal of Atmospheric and Oceanic Technology*, vol. 338, pp. 1701–1714, 2005.

[25] ——, "A bistatic phased-array Doppler sonar for wave-current research," *Journal of Atmospheric and Oceanic Technology*, vol. 31, pp. 1628–1641, 2014.

[26] M. D. Stokes and G. B. Deane, "A new optical instrument for the study of bubbles at high void fractions within breaking waves," *IEEE Journal of Oceanic Engineering*, vol. 24, pp. 300–311, 1999.
[27] D. T. Cox and S. Shin, "Laboratory measurements of void fraction and turbulence in the bore region of surf zone waves," *Journal of Engineering Mechanics*, pp. 1197–1205, 2003.
[28] I. Leifer, G. D. Leeuw, and L. H. Cohen, "Optical measurement of bubbles: System," *Journal of Atmospheric and Oceanic Technology*, vol. 20, pp. 1317–1332, 2003.
[29] C. D. Serdula and M. R. Loewen, "Experiments investigating the use of fibre-optic probes for measuring bubble-size distributions," *IEEE Journal of Oceanic Engineering*, vol. 23, pp. 385–399, 1998.
[30] C. E. Blenkinsopp and J. R. Chaplin, "Void fraction measurements in breaking waves," ser. 2088, vol. 463. Proceedings of the Royal Society of London Series A - Mathematical Physical and Engineering Sciences, 2007, pp. 3151–3170.
[31] ——, "Bubble size measurements in breaking waves using optical fiber phase detection probes," *IEEE Journal of Oceanic Engineering*, vol. 35, 2, pp. 388–401, 2010.
[32] C. J. Galvin, "Breaker type classification on three laboratory beaches," *Journal of Geophysical Research*, vol. 73, pp. 3651–3659, 1968.
[33] ——, "Breaker travel and choice of design wave height," *Journal of the Waterways and Harbours Division, ASCE, WW2*, vol. 95, pp. 175–200, 1969.
[34] E. R. Smith and N. C. Kraus, "Laboratory study of wave breaking over bars and artificial reefs," *Journal of Waterway, Port, Coastal and Ocean Engineering*, vol. 117, pp. 307–325, 1991.
[35] ——, "X-ray PTV measurement of solitary waves," vol. 367. 18th International Symposium on the Application of Laser and Imaging Techniques to Fluid Mechanics, 2016, pp. 2604–2612.
[36] M. Landrini, A. Colagrossi, M. Greco, and M. P. Tulin, "Griddless simulations of splashing processes and near-shore bore propagation," *Journal of Fluid Mechanics*, vol. 591, pp. 183–213, 2007.
[37] K. Zheng, Z. Sun, J. Sun, Z. Zhang, G. Yang, and F. Zhou, "Numerical simulations of water wave dynamics based on SPH methods," *Journal of Hydrodynamics*, vol. 21, pp. 843–850, 2009.
[38] K. Martins, C. Blenkinsopp, H. E. Power, B. Bruder, J. A. Puleo, and E. Bergsma, "High-resolution monitoring of wave transformation in the surf zone using a lidar scanner array," *Coastal Engineering*, vol. 128, pp. 37–43, 2017.
[39] P. C. M. Jansen, "Laboratory observations of the kinematics in the aerated region of breaking waves," *Coastal Engineering*, vol. 9, pp. 453–477, 1986.
[40] D. H. Peregrine, "The fascination of fluid mechanics," *Journal of Fluid Mechanics*, vol. 106, pp. 59–80, 1981.
[41] R. L. Miller, "Role of vortices in surf zone prediction: Sedimentation and wave forces," *Beach and Nearshore Sedimentation, Society of Economic Paleantologists and Mineralogists, Special Publication*, vol. 24, 1976.
[42] K. Nadaoka, "A fundamental study on shoaling and velocity field structure of water waves in the nearshore zone," Ph.D. dissertation, Tokyo Institute of Technology, Tokyo, 1986.
[43] K. Nadaoka, A. Hino, and Y. Koyano, "Turbulent flow field structure of breaking waves in the surf zone," *Journal of Fluid Mechanics*, vol. 204, pp. 359–387, 1989.
[44] P. Bonmarin, "Geometric properties of deep-water breaking waves," *Journal of Fluid Mechanics*, vol. 209, pp. 405–433, 1989.
[45] J. R. Tallent, T. Yamashita, and Y. Tsuchiya, *Transformation Characteristics of Breaking Water Waves*, a torum ot gudmestad ed. Kluwer Academic Publishers, 1990.
[46] B. L. D. S. Roman-Blanco, T. T. Coates, P. Holmes, A. J. Chadwick, A. Bradbury, T. E. Baldock, A. Pedrozo-Acuna, J. Lawrence, and J. Grüne, "Large scale experiments on gravel and mixed beaches: experimental procedure, data documentation and initial results," *Coastal Engineering*, vol. 53, pp. 349–362, 2006.
[47] S. Vagle and D. M. Farmer, "The measurement of bubble-size distributions by acoustical backscatter," *Journal of Atmospheric and Oceanic Technology*, vol. 9, no. 5, pp. 630–644, 1992.
[48] K. Govender, M. J. Alport, G. Mocke, and H. Michallet, "Video measurements of fluid velocities and water levels in breaking waves," *Physica Scripta*, vol. T97, pp. 152–159, 2002.
[49] J. Szczuka, "Acoustic detection of gas bubbles in the sea," *Oceanologia*, vol. 28, pp. 103–113, 1989.
[50] I. Leifer, R. K. Patro, and P. Bowyer, "A study on the temperature variation of rise velocity for large clean bubbles," *Journal of Atmospheric and Oceanic Technology*, vol. 17, pp. 1392–1402, 2000.

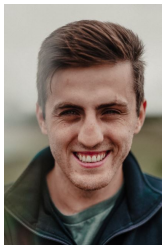

Oscar Bryan completed a M.Eng. degree in mechanical engineering from the University of Bath, U.K., in 2017. During the summer of 2016 he was an intern at Blueprint Subsea, U.K., and during the summer of 2017 he was a research assistant at the University of Bath. Since November 2017, Mr Bryan has been working as an automotive engineer at Federal Mogul Friction Products Ltd., U.K.

Paul M. Bayle completed a two-year degree in Civil Engineering at the University of Paul Sabatier, Toulouse, France, in 2011; a B.Sc. degree in Earth and Environment Science at the University of Bordeaux, France in 2012; and an M.Sc. degree in Oceanography at the University of Southampton, U.K., in 2014. He joined the Water Informatics and Science of Engineering (WISE) Centre for Doctoral Training (CDT) scheme in 2015 and is currently in the second year of his PhD based in the Department of Architecture and Civil Engineering at the University of Bath.

Christopher E. Blenkinsopp received the M.Eng. degree in civil engineering from the University of Nottingham, Nottingham, U.K., in 2001, and the Ph.D. degree in coastal hydrodynamics from the University of Southampton, Southampton, U.K., in 2007. From 2007 to 2013 he worked at the University of New South Wales, Australia, first as a research associate and then as a lecturer in water engineering. Since 2013, Dr Blenkinsopp has been a senior lecturer in the Department of Architecture and Civil Engineering at the University of Bath. Dr Blenkinsopps research focuses on coastal science and engineering.

Alan J. Hunter received the B.E.(Hons) and Ph.D. degrees in Electrical and Electronic Engineering from the University of Canterbury, New Zealand, in 2001 and 2006. From 2007 to 2010, he was a Research Associate at the University of Bristol, UK, and from 2010 to 2014 he was a Defense Scientist at TNO (Netherlands Organisation for Applied Scientific Research), The Netherlands. In 2014, Dr. Hunter joined the Faculty of Engineering at the University of Bath, UK, where he is currently a Senior Lecturer. Since 2017, he has been an Adjunct Associate Professor in the Department of Informatics at the University of Oslo, Norway. In 2018, he became an Associate Editor for IEEE Journal of Oceanic Engineering. Dr. Hunter's research interests are in underwater acoustics, sonar imaging of the seafloor, and autonomous underwater systems.